ADVANCES IN ATMOSPHERIC SCIENCES, VOL. 31, SEPTEMBER 2014, 1090–1100

Effect of Tropical Cyclone Intensity and Instability on the Evolution of Spiral Bands

HUANG Hong[1,2], JIANG Yongqiang[*1,2], CHEN Zhongyi[2], LUO Jian[2], and WANG Xuezhong[2]

[1]*Key Laboratory of Mesoscale Severe Weather, Ministry of Education of China, and School of Atmospheric Sciences, Nanjing University, Nanjing* 210093

[2]*College of Meteorology and Oceanography, PLA University of Science and Technology, Nanjing* 211101

(Received 25 May 2013; revised 9 December 2013; accepted 15 January 2014)

ABSTRACT

The evolution of spiral-band-like structures triggered by asymmetric heating in three tropical-cyclone-like vortices of different intensities is examined using the Three-Dimensional Vortex Perturbation Analyzer and Simulator (3DVPAS) model. To simulate the spiral bands, asymmetric thermal perturbations are imposed on the radius of maximum wind (RMW) of vortices, which can be considered as the location near the eyewall of real tropical cyclones (TCs).

All the three vortices experience a hydrostatic adjustment after the introduction of thermal asymmetries. It takes more time for weaker and stable vortices to finish such a process. The spiral-band-like structures, especially those distant from the vortex centers, form and evolve accompanying this process. In the quasi-balance state, the spiral bands are gradually concentrated to the inner core, the wave behavior of which resembles the features of classic vortex Rossby (VR) waves.

The unstable vortices regain nonhydrostatic features after the quasi-balance stage. The spiral bands further from the vortex center, similar to distant spiral bands in real TCs, form and maintain more easily in the moderate basic-state vortex, satisfying the conditions of barotropic instability. The widest radial extent and longest-lived distant bands always exist in weak and stable vortices.

This study represents an attempt to determine the role of TC intensity and stability in the formation and evolution of spiral bands via hydrostatic balance adjustment, and provides some valuable insights into the formation of distant spiral rainbands.

Key words: tropical cyclone, spiral band, hydrostatic balance adjustment, vortex

Citation: Huang, H., Y. Q. Jiang, Z. Y. Chen, J. Luo, and X. Z. Wang, 2014: Effect of tropical cyclone intensity and instability on the evolution of spiral bands. *Adv. Atmos. Sci.*, **31**(5), 1090–1100, doi: 10.1007/s00376-014-3108-5.

1. Introduction

As suggested by infrared imagery and radar reflectivity images, many tropical cyclones (TCs) exhibit some structural asymmetries. In addition to the storm size, structural forecasting is further complicated by such asymmetries. If a TC is described as the sum of a large axisymmetric component and a more varying asymmetric component (Shapiro, 1996; Pendergrass and Willoughby, 2009), its overall structure and intensity evolution may change as a result of the complicated interactions between the axisymmetric and asymmetric components. The rapid decaying of higher-wavenumber disturbances in the vicinity of the vortex core helps explain the robustness of storms (Carr and Williams, 1989; Smith and Montgomery, 1995). The decaying vortex Rossby (VR) waves are found to continuously amplify the growing discrete mode through the production of perturbation vorticity via their interaction with the basic-state vorticity gradient (Nolan and Montgomery, 2000).

Spiral rainbands are among the most important asymmetric components in TCs. According to their characteristics and location, they can always be classified into inner and outer bands (Guinn and Schubert, 1993; Wang, 2009). The inner bands lie close to the vortex center and the outer bands are typically located more than 500 km away from the vortex center and can be quite long and narrow. The inner rainbands are characterized by convectively coupled VR waves and the movement of the outer rainbands follows the low-level winds associated with the azimuthally-averaged low-level flow and the radially-outward cross-band flow caused by the downdraft-induced cold pool in the boundary layer (Li and Wang, 2012).

Houze (2010) divided rainbands into three basic types: distant, principle, and secondary rainbands. Distant rainbands are bands of convective clouds occurring entirely in the outer reaches of the storm. A principle rainband is a quasi-stationary feature that spirals inward from the outer reaches of the cyclone until it becomes roughly tangent to the eyewall (Willoughby, 1988). Secondary rainbands are located in the

* Corresponding author: JIANG Yongqiang
Email: jyq012@sina.com

inner core of the storm and have mesoscale kinematic characteristics consistent with VR waves (e.g., Montgomery and Kallenbach, 1997).

Spiral rainbands are often used to diagnose the current intensity and to forecast the future evolution of TCs (Atlas et al., 1963; Dvorak, 1975). This is because they are not only distinct features of a TC, but also may modulate the TC structure and intensity through one or more physical processes (Cione et al., 2000; Chen and Yau, 2001; Kimball, 2006; Franklin et al., 2006; Wang and Xu, 2010; Xu and Wang, 2010a, 2010b). The effects of spiral rainbands on the hurricane wind field are caused by the direct response to diabatic heating in their convection; and the response of the hurricane wind field to the rainband heating is, in the linear limit, the sum of the asymmetric potential vorticity (PV) and symmetric transverse circulations (Moon and Nolan, 2010). Cooling in the outer spiral rainbands maintains both the intensity of a TC and the compactness of its inner core, whereas heating in the outer spiral rainbands decreases the intensity but increases the size of a TC (Wang, 2009).

The growth of disturbances associated with instability of the symmetric hurricane vortex is a cause for polygonal eyewalls and the formation of mesovortices within or near the hurricane eye region (Schubert et al., 1999). Spiral rainbands can be triggered by the interaction between thermal perturbation and basic flow (Zhang et al., 2010). Under the influence of asymmetric thermal forcing similar to cumulus convection heating, the triggered gravity wave pulses result in new PV, which spreads toward the vortex core and then accumulates near the vortex core within the radius of maximum winds (RMW). The PV anomalies may be considered as the sources of spiral bands. However, the effects of symmetric basic vortices, especially their intensity and stability, on the evolution of asymmetric spiral bands are still unresolved.

In this paper, a three-dimensional, nonhydrostatic, linear numerical model of vortex dynamics is used to examine the role of TC intensity and instability on the evolution of spiral bands. Section 2 provides a brief introduction to the model. Section 3 describes three TC-like vortices of different intensities and the asymmetric thermal perturbations to be imposed. Section 4 analyzes the relationship between the hydrostatic balance adjustment and the evolution of spiral-band-like structures and compares the evolution of asymmetric perturbations in the basic-state vortices of different intensities. A summary and discussion are provided in section 5.

2. Numerical model

To simulate the evolution of asymmetric perturbations on TC-like vortices, the Three-Dimensional Vortex Perturbation Analysis and Simulation (3DVPAS) model is used in this paper, which is based on the vortex-anelastic equations in cylindrical coordinates on the f-plane (Hodyss and Nolan, 2007). It allows for the simulation and analysis of perturbations on axisymmetric, balanced vortices. The perturbations can have arbitrary structures in the radial and vertical directions, but vary harmonically in the azimuthal direction. Further details of 3DVPAS can be found in Nolan and Montgomery (2002, hereafter NM02), Nolan and Grasso (2003), and Nolan et al. (2007). The domain size of all simulations in this study is 300 km in the radial direction, covering 121 grids, and 20 km (31 levels) in the vertical direction. The grid stretching methodology is used to make the grid size a small but almost constant (approximately 1.2 km) interior to the RMW, which we shall refer to as the inner core region, and large in the outer region. The largest grid size is about 4.4 km.

3. Basic-state vortices and asymmetric perturbations

3.1. *Basic-state vortices*

The tangential wind fields of TCs, also called the basic-state vortices, are often represented by idealized profiles, which are frequently considered as in gradient wind and hydrostatic balance (Willoughby et al., 2006). In this study, we construct three idealized TC-like vortices of varying intensities by smoothly connecting piecewise constant vorticity profiles with cubic Hermite polynomials as in Eq. (3.1) in NM02, which are named as the Category 3 (C3), Category 1 (C1) and Tropical Storm (TS) vortex, respectively. The surface profiles of vorticity and velocity for the three basic-state vortices are shown in Fig. 1 in NM02. The C3 vortex has maximum wind speed of 54.2 m s^{-1} at the RMW of 34.5 km, and maximum vorticity of 5.3×10^{-3} s^{-1} at the radius of maximum vorticity (hereafter RMV) of 26.0 km. The C1 vortex has maximum wind speed of 36.0 m s^{-1} at the RMW of 42.5 km, and maximum vorticity of 2.5×10^{-3} s^{-1} at the RMV of 28.0 km. The TS vortex has maximum wind speed of 21.5 m s^{-1} at the RMW of 49.0 km, and maximum vorticity of 1.5×10^{-3} s^{-1} at the vortex center. In order to study all three vortices in the same computational domain, the TS vortex may be smaller than the real ones. More detailed descriptions about the three vortices are shown in NM02.

The C3 vortex is the strongest one and the TS vortex is the weakest. Moreover, their stabilities are different. Both the C3 and C1 vortices are unstable to low azimuthal-wavenumber (n) perturbations. The C3 vortex is most unstable for $n = 3$, with an e-folding time of about 1.34 h. For the C1 vortex, the most unstable mode occurs for $n = 2$, with an e-folding time of approximately 5.51 h (NM02). The growth rate of the C3 vortex is much larger than the C1 vortex. The weakest TS vortex was found to be stable for all azimuthal-wavenumbers. More dynamical instability analysis can be found in Zhang et al. (2010).

3.2. *Asymmetric thermal perturbations*

Localized bursts of convection, frequently observed in the inner core of developing TCs, constitute the dominant energy source for TCs (NM02), which may be the energy source for the formation of spiral rainbands in real TCs (Chen et al., 2010). In order to represent the immediate effect of a burst of

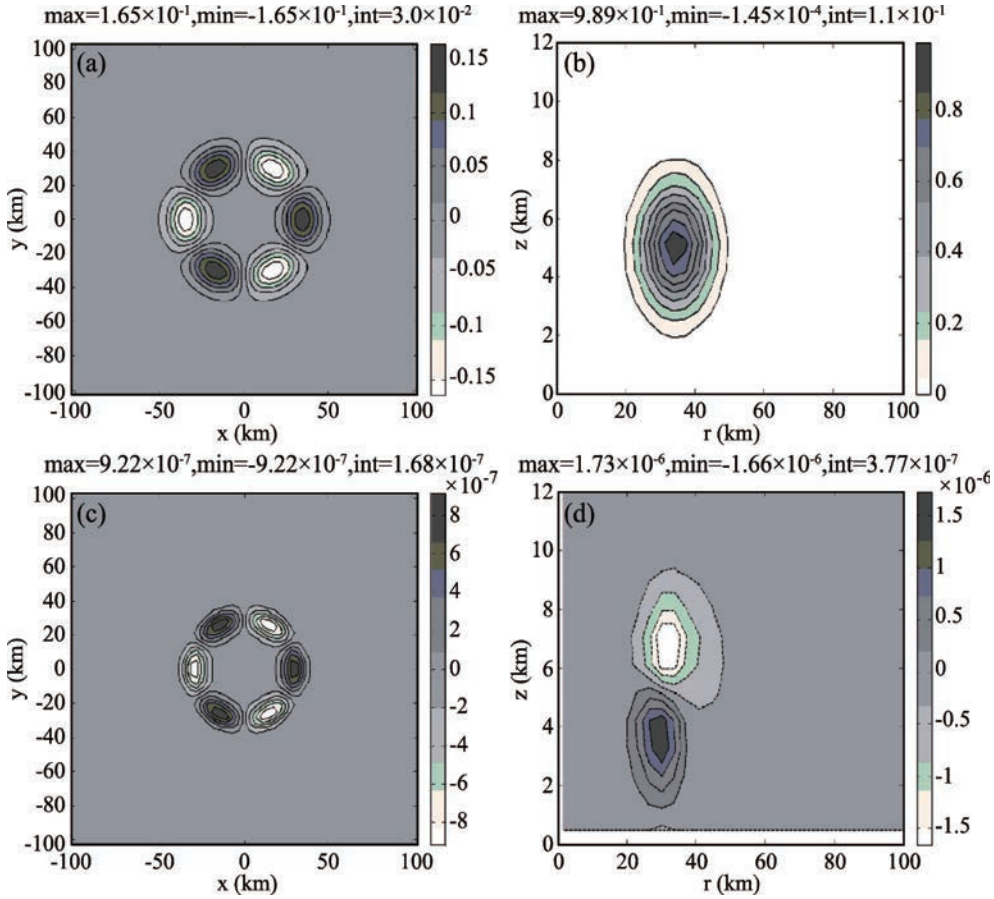

Fig. 1. Horizontal and vertical cross sections of initial θ (units: K) and PV (units: m^2 K s^{-1} kg^{-1}) perturbations in the C3 vortex: (a) horizontal cross section of θ; (b) vertical cross section of θ; (c) horizontal cross section of PV; and (d) vertical cross section of PV.

convection in a TC, a pure and unbalanced thermal perturbation is imposed on the basic-state field as initial conditions in the 3DVPAS model. The thermal perturbation, i.e. a thermal bubble is defined in a similar way to NM02, i.e.,

$$\theta_n(r,z,t=0)=\theta_0\exp\left[-\left(\frac{r-r_b}{\sigma_r}\right)^2-\left(\frac{z-z_b}{\sigma_z}\right)^2\right], \quad (1)$$

where r is the radius from the vortex center, z is the altitude from the surface, and t is the time; θ is the potential temperature; $\theta_0 = 1.0$ K is the amplitude of maximum potential temperature (θ) anomaly; r_b and z_b are the radial and altitude location of the thermal bubble center, $\sigma_r = 20$ km is the radial half-width and $\sigma_z = 2$ km is the vertical half-width of the thermal bubble, wherein subscript b is the abbreviation of bubble, subscript r and z denote radial and vertical half-width of the bubble, respectively. In this study, $z_b = 5$ km, $r_b = R_{max}$, where R_{max} is the RMW for each of the three vortices (NM02). Based on the instability analysis, we consider the perturbations for $n = 3$ for the C3 vortex, $n = 2$ for the C1 vortex, and $n = 2$ for the TS vortex in this study.

The horizontal and vertical cross section of initial θ imposed on the C3 vortex at $z = 2.33$ km is shown in Figs. 1a and b. Supposing there is initially no motion, the initial thermal perturbation defined in Eq. (1) accounts for the titled meridional structure of the initial PV anomalies shown in Figs. 1c and d. The values of PV are approximately positive (negative) below (above) 5 km (NM02).

Similar perturbations were superposed by NM02 to the TS and C1 vortex to compare their asymmetric adjustment processes. The inner-core structure and dynamics were mainly discussed in their paper. We focus mainly on the asymmetric perturbations related to the spiral-band-like structures, and thus their evolution in the whole simulation domain is discussed in the following section.

4. Results and analysis

4.1. *Hydrostatic balance adjustment*

In order to compare the spiral band behaviors during the hydrostatic balance adjustments in different symmetric vortices, we investigate the features of the adjustment processes within them. At the beginning, the basic vortices satisfy hydrostatic balance, but such balance might be broken by the change of potential temperature via the buoyancy term according to the vertical momentum equation, which is confirmed by comparing the full pressure field to the hydrostatic

pressure field as proposed by NM02. The hydrostatic pressure fields are derived from the potential temperature by integrating

$$\frac{\partial p_n}{\partial z} = \bar{\rho} g \frac{\theta_n}{\theta} , \tag{2}$$

where $\bar{\rho} = \bar{\rho}(r,z)$ is the anelastic density field, which does not change with time; g is the gravity acceleration, and the expression for p_n is presented in Appendix A by NM02. The nonhydrostatic feature can be evaluated by the root-mean-square difference (RMSD) between the full and hydrostatic pressure field, volume-weighted over the domain, as a function of time.

Figure 2 illustrates the evolution of RMSD between the full and hydrostatic pressure fields for the three vortices. The evolution of unstable vortices, such as the C3 and C1 vortices, can be divided into three basic steps. Initially, the RMSDs are very large and then decrease abruptly, which corresponds to the adjustment processes that were attributable to the introduction of unbalanced thermal perturbations. The RMSD of the C3 vortex is very large before 0.5 hours (Fig. 2b), and then decreases to a relatively steady minimum value after a little more than an hour. It takes about 10 hours for the C1 vortex to finish this process (Fig. 2c). The RMSDs of the two vortices remain relatively steady in the second step, which corresponds to a quasi-hydrostatic state. However, such a quasi-balanced feature cannot be sustained, and the RMSDs ultimately increase abruptly and reach a value in the order of the initial extreme value at approximately $t = 3$ h for the C3 vortex, and 30 h for the C1 vortex.

The 3DVPAS model satisfies the anelastic incompressibility condition (NM02), so acoustic waves are filtered. Gravity waves might play an important role in dispersing the imbalance resulting from thermal perturbations and return the vortices to a quasi-balanced state (Ye and Li, 1965). Accordingly, the convection and the ensuing adjustment processes generate ubiquitous gravity waves in real TCs (Moon and Nolan, 2010). The superposed perturbations are transient, so the hydrostatic balance state will be affected by the nonlinear advection and friction. An arbitrary small perturbation may grow substantially as a result of the instability of basic-state vortices, which will in turn enhance the nonlinear effects and the departures from the hydrostatic balance state. Therefore, the unstable vortices restore nonhydrostatic features in the third step of the evolution, much faster for stronger vortices (Figs. 2a and c). The perturbations in a stable vortex might be neutral or decaying, so nonlinear advection in such a vortex will not increase with time. The RSMD for the TS vortex decreases continually after the initial adjustment, taking about 6 hours as shown in Fig. 2d. Then, it tends toward zero after $t = 14$ h in the simulation, ultimately confirming the hydrostatic feature.

4.2. *Evolution of asymmetric perturbations*

Shortly after the introduction of thermal perturbations, secondary cells appear arranged in bands around the center of the C3 vortex, in addition to compact regions of vertical air movement surrounding its RMW, where the thermal perturbations are imposed (Fig. 3a). These bands spiral into

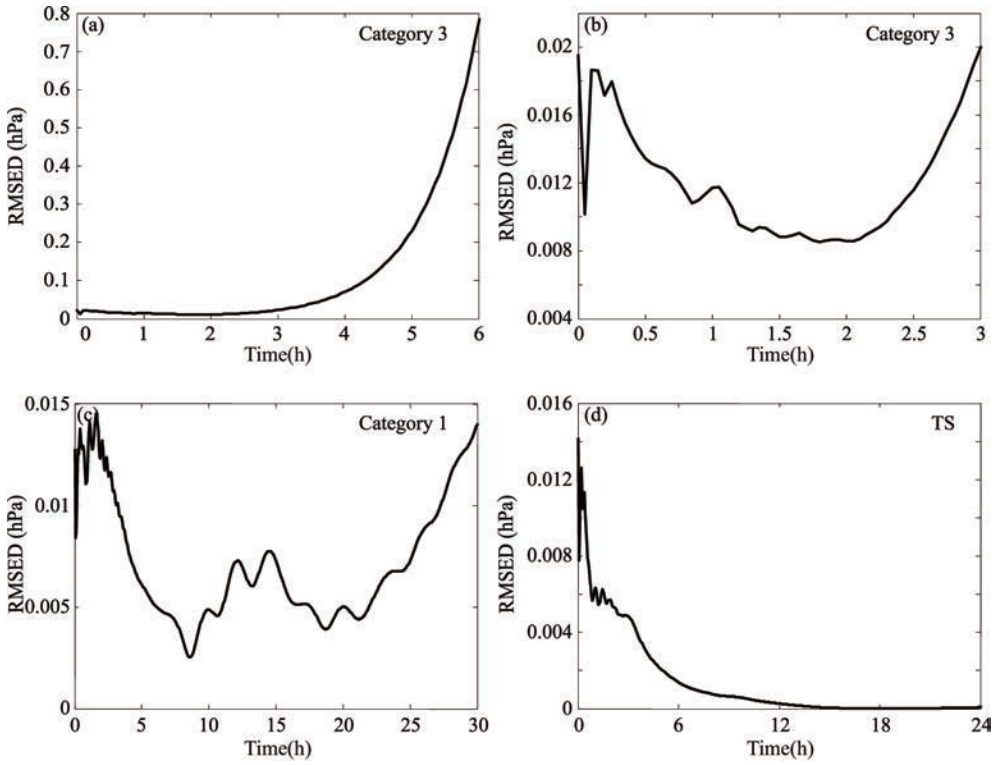

Fig. 2. Evolution of RMSDs (units: hPa) between the full and hydrostatic pressure fields in three vortices as a function of time.

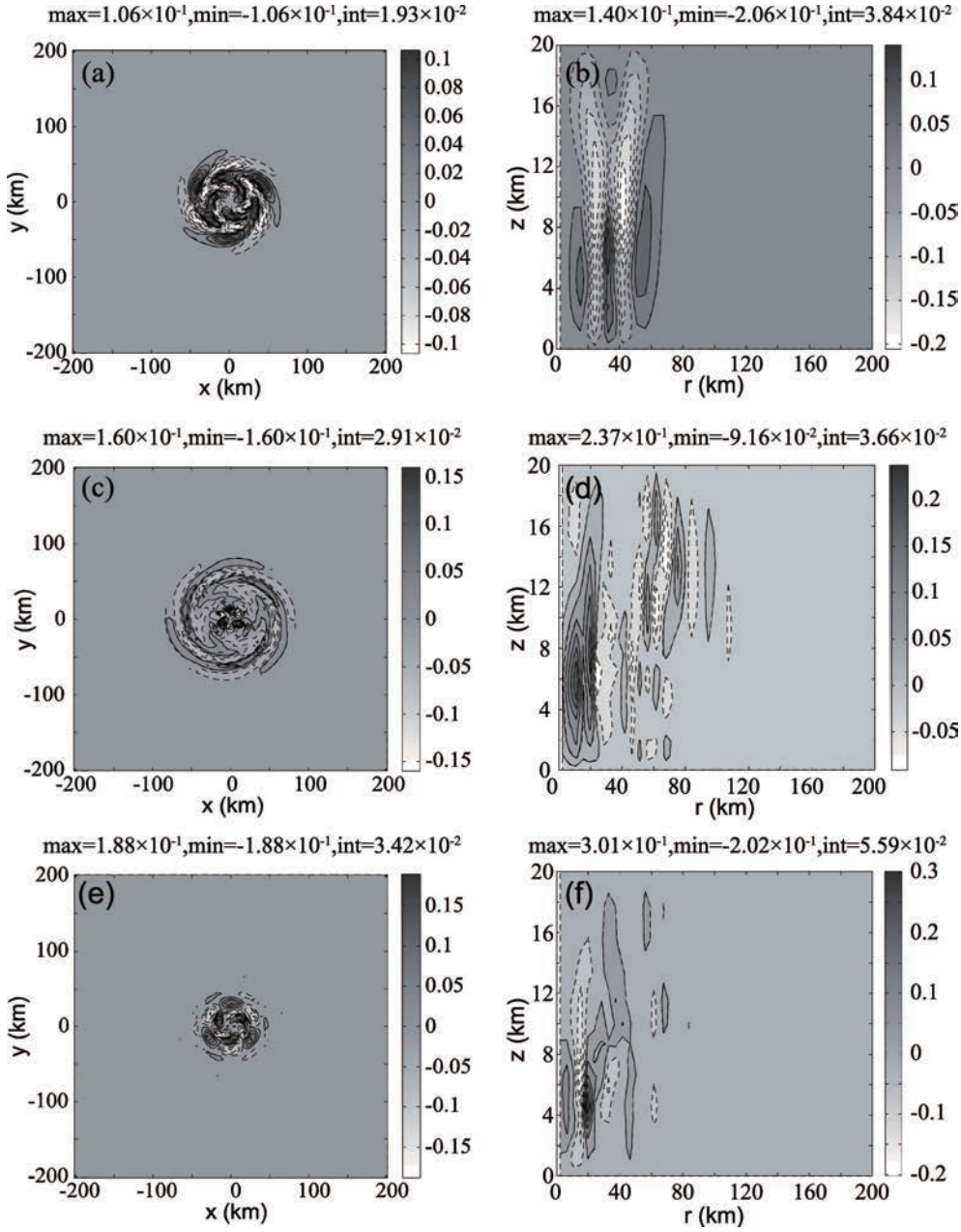

Fig. 3. Horizontal cross section of the vertical velocity anomalies at $z = 2.33$ km (units: m s^{-1}) at (a) $t = 0.15$ h, (c) $t = 0.6$ h, and (e) $t = 2.0$ h, and vertical section of the vertical velocity anomalies at (b) $t = 0.15$ h, (d) $t = 0.6$ h, and (f) $t = 2.0$ h in the C3 vortex.

the center of the vortex. The air ascends and descends alternately along the radial direction and the vertical velocity fields show nonzero-wavenumber properties in the vertical direction at the radius near the RMW (Fig. 3b). The behavior of the perturbations is in direct contrast to NM02, who showed that the most unstable mode in the C3 vortex is made up of two concentric sets of perturbations that lie on either side of the RMV (also where the vorticity gradient changes sign). They interpreted such a mode as a discrete VR wave. The sign change in the radial gradient of the C3 vortex satisfies the necessary conditions for barotropic instability, so the unstable mode represents the properties of traditional coupled VR–VR wave barotropic instability, as shown in Fig. 1a by Hodyss and Nolan (2008), who provided a comprehensive comparison between Rossby-inertial-buoyancy (RIB) waves and traditional coupled VR–VR wave barotropic instability. In this paper, the behavior of VR waves undergoing inertial-buoyancy (IB) wave emission on vortices with baroclinic vertical structures is studied using a radially modified form of anelastic momentum equations in cylindrical coordinates, as in Hodyss and Nolan (2007) and NM02. In our simulations, the introduction of thermal perturbations also makes the wave property different from the traditional VR waves.

Accompanying the adjustment processes, the vertical

velocity field exhibits obvious spiral-band-like structure at around the 100-km radial extent, and there are several vertical movement centers within the spiral band, with the most intense upward movement appearing close to the RMW (Fig. 3c). The perturbation structure has been divided into inner and outer parts by the RMW of C3. The inner part can be identified as a VR wave, and it peaks near the MRV of C3. In the outer region, the perturbation is a spiral wave that propagates away from the vortex, which can be identified as an IB wave. The behavior of the IB wave is verified by the nonzero-vertical-wavenumber features of vertical velocity evident outside of the RMW of the basic-state vortex (Fig. 3d). As a whole, the perturbations resemble the properties of RIB waves, as shown in Fig. 4b by Hodyss and Nolan (2008).

The outer perturbations gradually weaken at the quasi-balanced stage, and the maximum vertical movement distributes within $r = 34.5$ km, namely within the MRV, which in real TCs is closely associated with an annulus of intense precipitation known as the eyewall, with an almost zero vertical wavenumber (Figs. 3e and f). The wave properties of perturbations are gradually dominated by the traditional coupled VR–VR wave barotropic instability. The anticlockwise and outward propagation fails to be maintained for 6 hours (Figs. 4a and b). The PV anomalies experience an unexpected increase after $t = 11$ h near the MRV, where the VR waves are phase-locked so as to amplify each other (NM02).

Both the C1 and C3 vortex are unstable, and they are

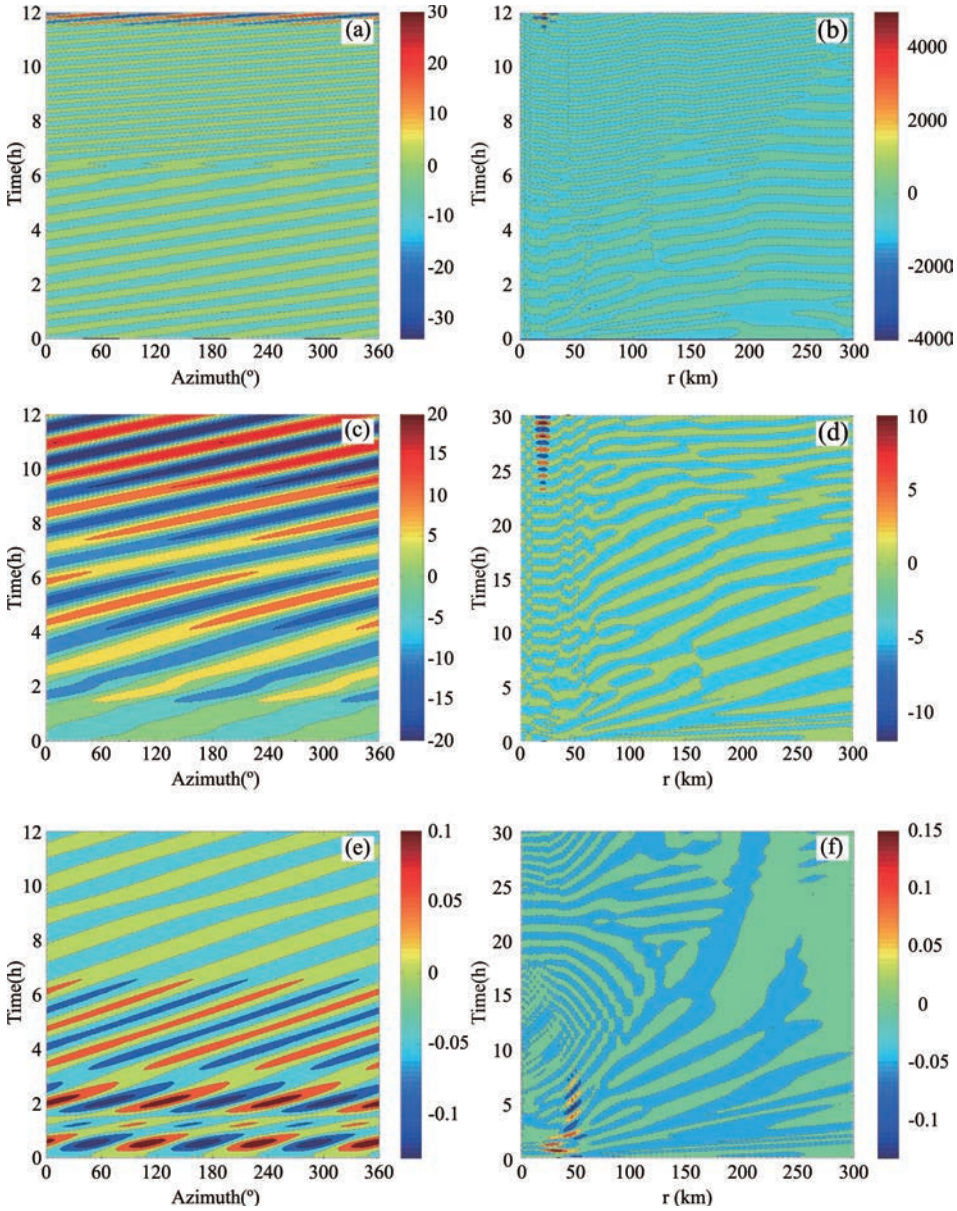

Fig. 4. Left column: azimuth–time Hovmoller diagram of PV anomalies (units: PVU) along the RMW for the (a) C3 vortex, (c) C1 vortex, and (e) TS vortex. Right column: radius–time Hovmoller diagram of PV anomalies for the (b) C3 vortex, (d) C1 vortex, and (f) TS vortex.

mainly different in intensity. Therefore, the perturbations to C1 experience similar evolution processes to those to C3. However, their structures are evidently different. The behavior of waves in the C1 vortex resembles the structure of a classic RIB mode immediately after the introduction of thermal perturbations (Fig. 5a). The vertical velocity fields exhibit a clear spiral-band shape with an almost 200-km radial extent after more than 2 hours (Fig. 5c). As shown by Fig. 2, it is difficult for C1 to maintain a quasi-balance stage, so the RIB property is retained for relatively longer than in C3. Accordingly, the spiral bands with wider radial extent can last for much more time (Fig. 5e). The transition of wave properties is also shown by the horizontal distribution of θ perturbations (Figs. 5b, d and f). The anticlockwise and outward propagation of perturbations to C1 are maintained for more than 20 hours (Figs. 4c and d). Finally, the wave properties are dom-

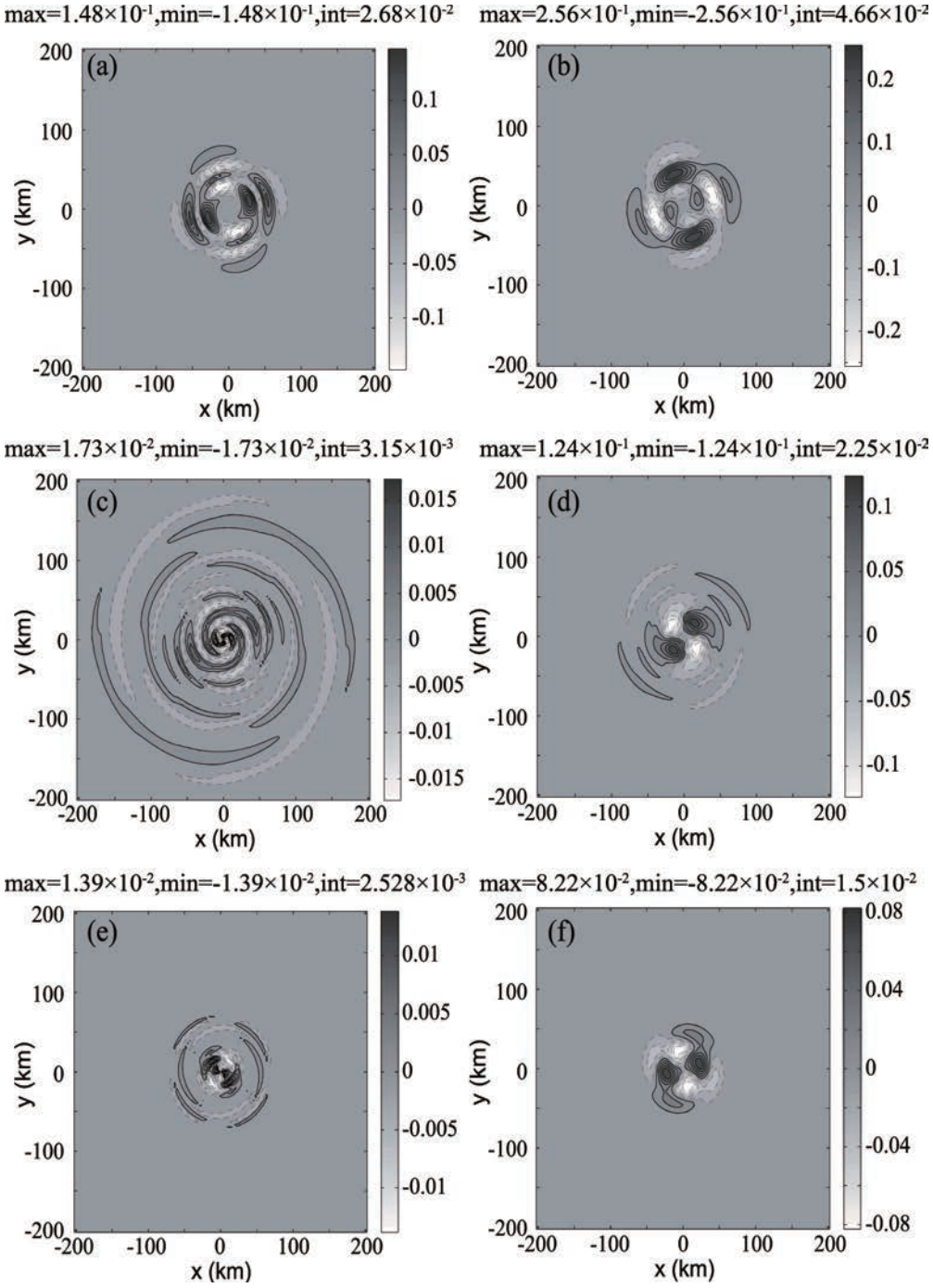

Fig. 5. Horizontal cross section of vertical velocity anomalies (units: m s^{-1}) at $z = 2.33$ km at (a) $t = 0.15$ h, (c) $t = 2.7$ h, and (e) $t = 5.0$ h, and θ anomalies (units: K) at (b) $t = 0.15$ h, (d) $t = 2.7$ h, and (f) $t = 5.0$ h in the C1 vortex.

inated by the traditional coupled VR waves, which are also phase-locked at the MRV of C1.

The TS vortex is a monotonic vortex, whose radial vorticity gradient does not change sign, so coupled VR wave instability on it is not possible. The evolution of asymmetries in the TS vortex was ever discussed in NM02, whereas a 3-wavenumber thermal perturbation was introduced into the outer core of the vortex in their study. The evolution of the perturbations also goes through two phases: a short-term evolution of internal gravity waves and a long-term phase described by the evolution of the resulting PV fields. In this study, the initial thermal perturbations are located near the RMW, but not 80 km from the vortex center as in NM02. Initially, the evident vertical movements are concentrated within 100 km from the vortex center (Fig. 6a) and the phases of vertical velocity are almost unchanged at all levels except the radius where upon the thermal perturbations are imposed (Fig. 7a). After 1 hour, the vertical velocity is characterized by a notable spiral-band structure with scale in the azimuthal direction larger than that in the radial direction (Fig. 6b). The vertical velocity maxima regions incline clearly outside $r = 50$ km with a distribution of alternately positive and negative values in the radial direction, while they incline very little within $r = 50$ km (Fig. 7b). The indication is that the vertical upward movements within the RMW are dominant, while the radial motions are evident outside of the RMW. The high values of vertical velocities almost distribute within the MRV with the integration. The spiral-band shape in the TS vortex is wider and has longer duration than those in both the C3 and C1 vortices (Figs. 6c and 7c). The vertical motions at upper and lower levels have the same direction within the RMW after 15 hours of integration (Figs. 6d and 7d).

The behavior of waves in the TS vortex, which is forced by the thermal asymmetries near its RMW, is in direct contrast with those in the C3 and C1 vortices. The waves are not dominated by VR waves, but resemble the horizontal structure of a classic RIB wave. The waves in the quasi-balanced stage are similar to those proposed by NM02, but without evident fish-shaped features in its inner core (Fig. 6b). The spiral bands triggered in the TS vortex are wider than those in the unstable C3 and C1 vortices, which rotate very slowly in the azimuthal direction and mainly propagate in the radial direction (Figs. 4e and f). Such bands become narrower with the development and contrast to the center (Fig. 6d). Comparable with C1 and C3, its extreme perturbations appear near the RMW before 6 hours of simulation.

In the unstable vortices, the inner VR waves might be coupled with the outer IB waves during the hydrostatic adjustment. In the strong C3 vortex, the PV anomalies are not yet dominated by the feature of VR waves (Figs. 8a and b). The waves at the quasi-balance stage resemble the features of classic VR waves (Figs. 8c and d). The existence of the IB wave favors the spiral-band-like structures with wider radial extent. It is difficult for the weaker, unstable vortex, e.g., C1, to regain quasi-balance, so the spiral bands further from the vortex center, similar to distant spiral bands in real TCs,

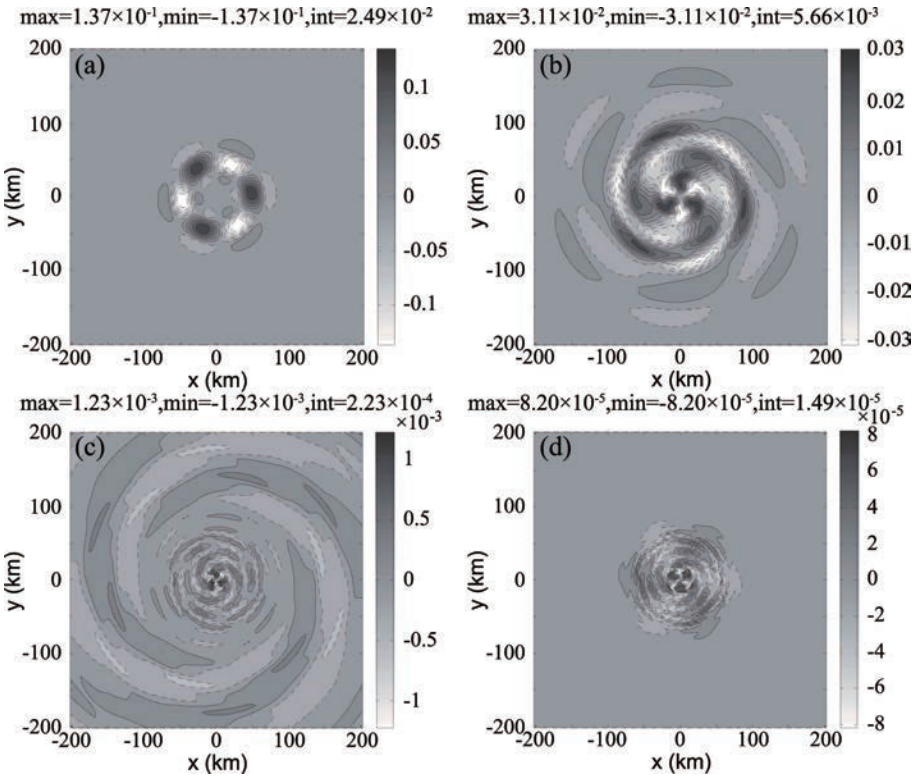

Fig. 6. Horizontal distribution of vertical velocity anomalies (units: m s^{-1}) at $z = 2.33$ km at (a) $t = 0.2$ h, (b) $t = 1.0$ h, (c) $t = 6.0$ h, and (d) $t = 15.0$ h in the TS vortex.

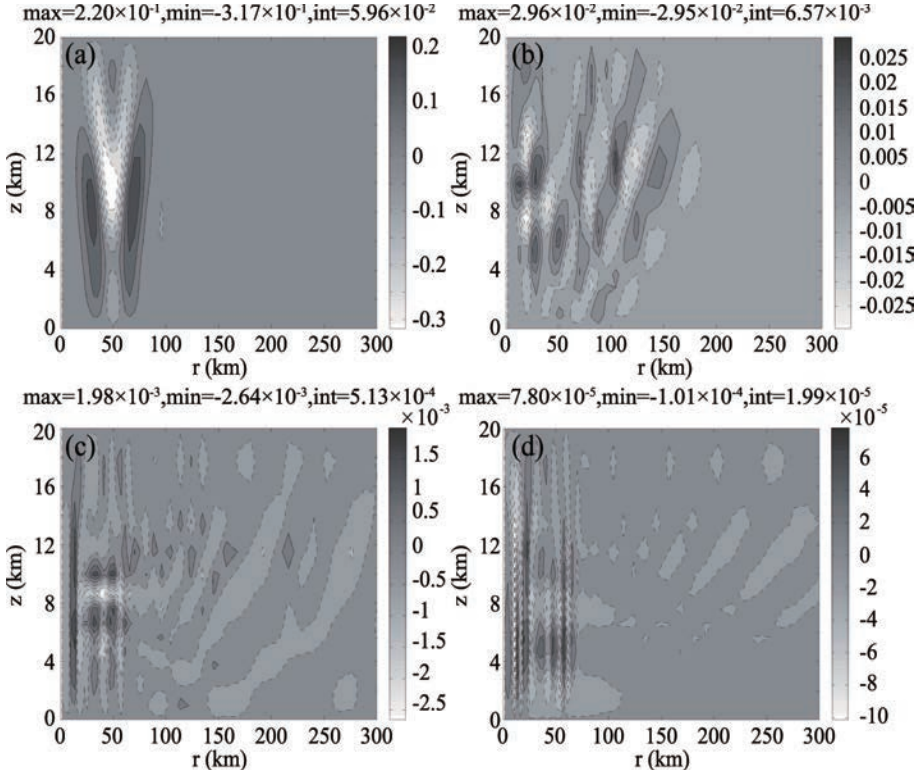

Fig. 7. Radius–height cross sections of vertical velocity anomalies (units: m s^{-1}) at (a) $t = 0.2$ h, (b) $t = 2.0$ h, (c) $t = 6.0$ h, and (d) $t = 15$ h in the TS vortex.

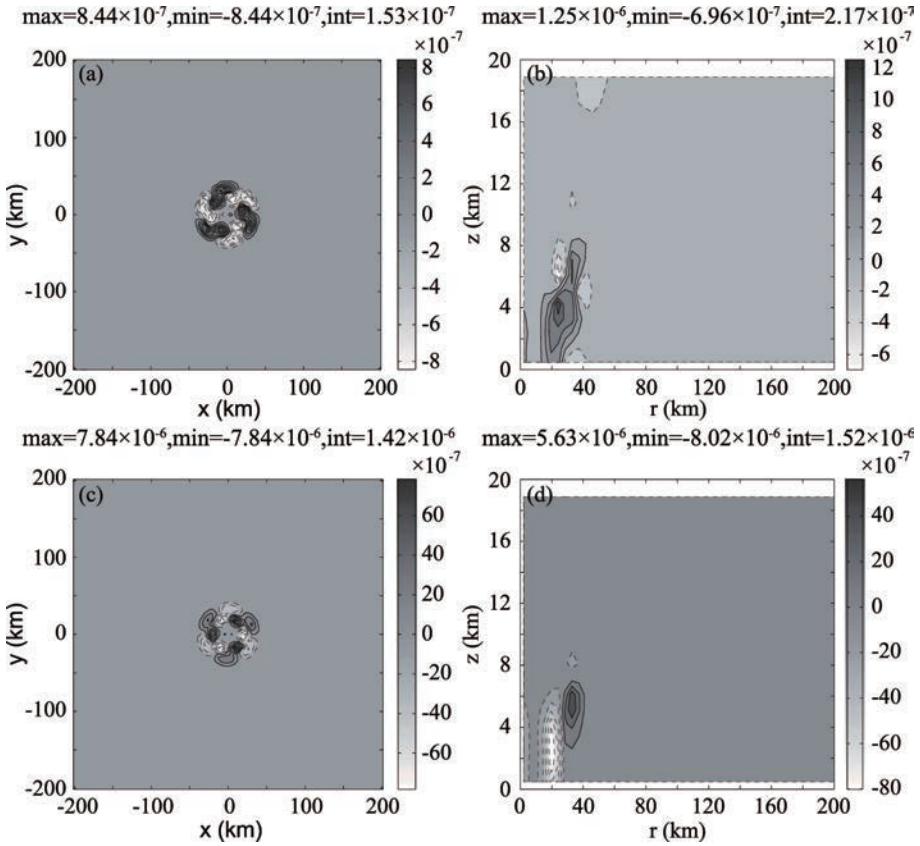

Fig. 8. Horizontal cross section of PV anomalies (units: m^2 K s^{-1} kg^{-1}) at $z = 2.33$ km in the C3 vortex at (a) $t = 0.5$ h and (c) $t = 2$ h; and radius–height cross section of PV anomalies at (b) $t = 0.5$ h and (d) $t = 2$ h.

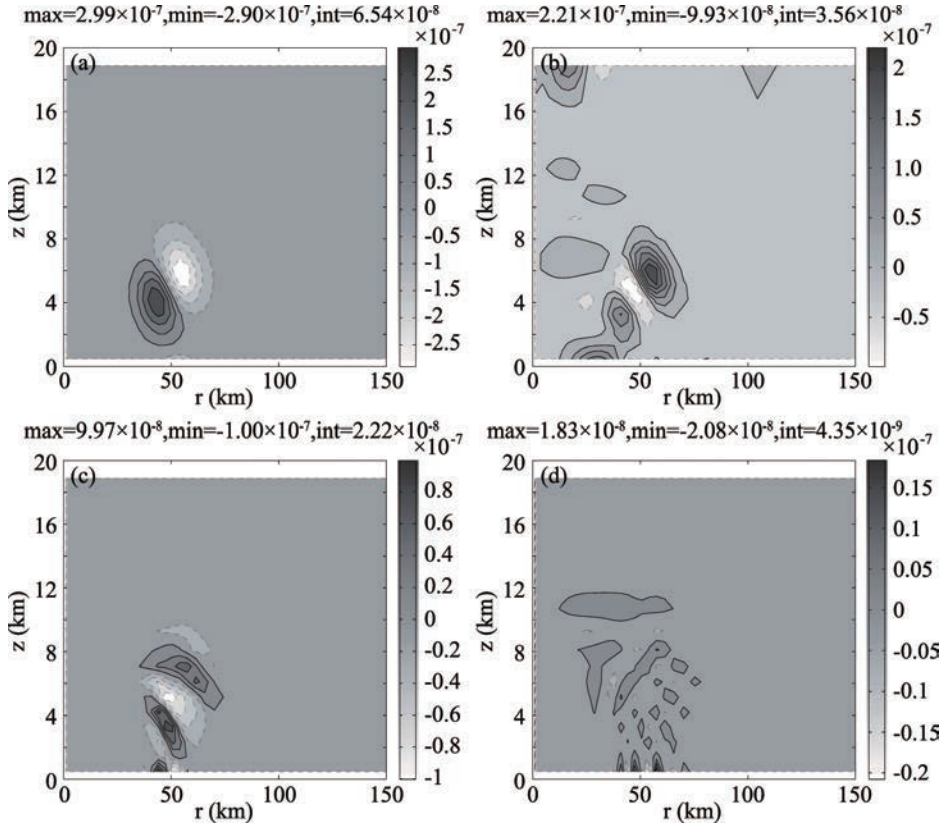

Fig. 9. Radius–height cross sections of PV anomalies (units: m^2 K s^{-1} kg^{-1}) in the TS vortex at (a) initial time, (b) $t = 1.25$ h, (c) $t = 5$ h, and (d) $t = 10$ h.

form and maintain more easily. Whereas, the stronger vortex might absorb the asymmetric perturbations to spiral rapidly into its centre, and a compact PV band forms near the RMV, which is similar to the structure of an eyewall-rainband complex (Houze, 2010). In the stable vortex, the RIB waves are triggered by the thermal asymmetries. The VR waves propagate outward (Figs. 9b and c) and favor the widest radial extent and longest-lived distant bands. The asymmetric perturbations are decaying and contract to the vortex center (Fig. 9d).

5. Discussion and conclusions

In this study, the TCs of different intensities were approximated by three categories of vortices and the defined thermal perturbations were respectively introduced into the RMWs of these vortices, which can be considered as the location near the eyewall of real TCs. For simplicity, we simulated the evolution of asymmetric perturbations using the 3DVPAS model to trace the evolution of spiral band-shape structures without considering the symmetric response.

The simulations show that all the three vortices experience a hydrostatic adjustment process after the introduction of thermal asymmetries, which is relatively faster in stronger vortices. Subsequently, the vortices maintain a quasi-balanced state for longer. The unstable vortices, such as the C3 and C1 vortices, ultimately regain a nonhydrostatic state.

Deep convection often occurs in the eyewall and spiral rainbands in real TCs. The thermal perturbations introduced into the vortex near the RMW in this simulation can, in part, represent the effect of pulse heating near eyewalls. In convection regions, the hydrostatic balance may be broken and resumed after a fast adjustment via the dispersion of gravity waves. The time taken for the hydrostatic balance adjustment to finish mainly depends on the instability and intensity of basic vortices. The formation of distant bands, which is considered to be much more complicated (Li and Wang, 2012), might accompany the process of hydrostatic balance adjustment. In the quasi-balance state, the spiral bands gradually concentrate to the inner core, which are commonly studied from the perspective of VR waves. This study represents an attempt to determine the role of TC intensity and stability in the formation of spiral bands via hydrostatic balance adjustment. This may enhance our understanding of the formation and evolution of distant spiral rainbands. However, in view of our linear model and oversimplified thermal asymmetries, our conclusions need to be verified in future work using numerical simulations.

Acknowledgements. The authors would like to thank Prof. David S. NOLAN for providing the 3DVPAS programs and many helpful suggestions during the course of this work. We are also grateful to Prof. WANG Y. and the three anonymous reviewers for their valuable suggestions. This research was supported

by the National Natural Science Foundation of China (Grant Nos. 40905021, 41375049 and 41275099), the Chinese Postdoctoral Science Foundation (Grant No. 2011M500894), and the R&D Special Fund for Public Welfare Industry (meteorology) (Grant No. GYHY201206005).

REFERENCES

Carr, L. E. III, and R. T. Williams, 1989: Barotropic vortex stability to perturbations from axisymmetry. *J. Atmos. Sci.*, **46**, 3177–3191.

Chen, X. J., H. Huang, Z. Y. Chen, and X. Z. Wang, 2010: A numerical simulation study on Typhoon Manyi spiral bands. *Meteorology and Disaster Reduction Research*, **33**, 9–15. (in Chinese with English abstract)

Chen, Y. S., and M. K. Yau, 2001: Spiral bands in a simulated hurricane. Part I: Vortex Rossby wave verification. *J. Atmos. Sci.*, **58**, 2128–2145.

Cione, J. J., P. G. Black, and S. H. Houston, 2000: Surface observations in the hurricane environment. *Mon. Wea. Rev.*, **128**, 1550–1561.

Dvorak, V. F., 1975: Tropical cyclone intensity analysis and forecasting from satellite imagery. *Mon. Wea. Rev.*, **103**, 420–430.

Franklin, C. N., G. J. Holland, and P. T. May, 2006: Mechanisms for the generation of mesoscale vorticity features in tropical cyclone rainbands. *Mon. Wea. Rev.*, **134**, 2649–2669.

Guinn, T. A., and W. H. Schubert, 1993: Hurricane spiral bands. *J. Atmos. Sci.*, **50**, 3380–3403.

Hodyss, D., and D. S. Nolan, 2007: Linear anelastic equations for atmospheric vortices. *J. Atmos. Sci.*, **64**, 2947–2959.

Hodyss, D., and D. S. Nolan, 2008: The Rossby-inertia-buoyancy instability in baroclinic vortices. *Phys. Fluids*, **20**, 096 602–096 621.

Houze, R. A, Jr., 2010: Clouds in tropical cyclones. *Mon. Wea. Rev.*, **138**, 293–344.

Kimball, S. K., 2006: A modeling study of hurricane landfall in a dry environment. *Mon. Wea. Rev.*, **134**, 1901–1918.

Li, Q. Q., and Y. Q. Wang, 2012: A comparison of inner and outer spiral rainbands in a numerically simulated tropical cyclone. *Mon. Wea. Rev.*, **140**, 2782–2805.

Montgomery, M. T., and R. J. Kallenbach, 1997: A theory for vortex Rossby-waves and its application to spiral bands and intensity changes in hurricanes. *Quart. J. Roy. Meteor. Soc.*, **123**, 435–465.

Moon, Y., and D. S. Nolan, 2010: The dynamic response of the hurricane wind field to spiral rainband heating. *J. Atmos. Sci.*, **67**, 1779–1805.

Nolan, D. S., and M. T. Montgomery, 2000: The algebraic growth of wavenumber one disturbances in hurricane-like vortices. *J. Atmos. Sci.*, **57**, 3514–3538.

Nolan, D. S., and M. T. Montgomery, 2002: Nonhydrostatic, three-dimensional perturbations to balanced, hurricane-like vortices. Part I: Linearized formulation, stability, and evolution. *J. Atmos. Sci.*, **59**, 2989–3020.

Nolan, D. S., and L. D. Grasso, 2003: Nonhydrostatic, three-dimensional perturbations to balanced, hurricane-like vortices. Part II: Symmetric response and nonlinear simulations. *J. Atmos. Sci.*, **60**, 2717–2745.

Nolan, D. S., Y. Moon, and D. P. Stern, 2007: Tropical cyclone intensification from asymmetric convection: Energetics and efficiency. *J. Atmos. Sci.*, **64**, 3377–3405.

Pendergrass, A. G., and H. E. Willoughby, 2009: Diabatically induced secondary flows in tropical cyclones. Part I: Quasi-steady forcing. *Mon. Wea. Rev.*, **137**, 805–821.

Senn, H. V., H. W. Hiser, 1959: On the origin of hurricane spiral rain bands. J. Meteor., **16**, 419–426.

Schubert, W. H., M. T. Montgomery, R. K. Taft, T. A. Guinn, S. R. Fulton, J. P. Kossin, and J. P. Edwards, 1999: Polygonal eyewalls, asymmetric eye contraction, and potential vorticity mixing in hurricanes. *J. Atmos. Sci.*, **56**, 1197–1223.

Shapiro, L. J., 1996: The motion of hurricane Gloria: A potential vorticity diagnosis. *Mon. Wea. Rev.*, **124**, 2497–2508.

Smith, G. B. II, and M. T. Montgomery, 1995: Vortex axisymmetrization: Dependence on azimuthal wave-number or asymmetric radial structure changes. *Quart. J. Roy. Meteor. Soc.*, **121**, 1615–1650.

Wang, Y. Q., 2009: How do outer spiral rainbands affect tropical cyclone structure and intensity? *J. Atmos. Sci.*, **66**, 1250–1273.

Wang, Y. Q., and J. Xu, 2010: Energy production, frictional dissipation, and maximum intensity of a numerically simulated tropical cyclone. *J. Atmos. Sci.*, **67**, 97–116.

Willoughby, H. E., 1988: The dynamics of the tropical hurricane core. *Aust. Meteor. Mag.*, **36**, 183–191.

Willoughby, H. E., R. W. R. Darling, and M. E. Rahn, 2006: Parametric representation of the primary hurricane vortex. Part II: A new family of sectionally continuous profiles. *Mon. Wea. Rev.*, **134**, 1102–1120.

Xu, J., and Y. Q. Wang, 2010a: Sensitivity of tropical cyclone inner-core size and intensity to the radial distribution of surface entropy flux. *J. Atmos. Sci.*, **67**, 1831–1852.

Xu, J., and Y. Q. Wang, 2010b: Sensitivity of the simulated tropical cyclone inner-core size to the initial vortex size. *Mon. Wea. Rev.*, **138**, 4135–4157.

Ye, D. Z., and M. C. Li, 1965: *Adjustment Issues of Atmosphere Motion*. Science Press, Beijing, 126 pp. (in Chinese)

Zhang, M., H. Huang, and L. F. Zhang, 2010: Atmospheric wave spectrum analysis and instability. 3rd ed., *Perturbations in Tropical Cyclone*, China Meteorological Press, Beijing, 238 pp. (in Chinese)